

Retinal nerve fiber layer reflectometry must consider directional reflectance

Xiang-Run Huang,* Robert W. Knighton, William J. Feuer, and Jianzhong Qiao

Bascom Palmer Eye Institute, Miller School of Medicine University of Miami, Miami, FL 33136, USA

**xhuang3@med.miami.edu*

Abstract: Recent studies reveal that measurements of retinal nerve fiber layer (RNFL) reflectance provide more sensitive detection of glaucomatous damage than RNFL thickness, but most do not consider directional reflectance of the RNFL, an important source of variability. This study quantitatively compared RNFL directional reflectance, represented by an angular spread function (ASF), measured at different scattering angles, different wavelengths and different distances from the optic nerve head (ONH) and for bundles with different thicknesses (**T**). An ASF was characterized by its amplitude (**A**) and width (**W**). Internal reflectance of a bundle was expressed as **A/T**. The study found that **A** varied significantly with scattering angle and wavelength and that **A/T** was different among bundles but constant along the same bundle, indicating that the internal structure of axons may vary among bundles but does not change with distance. This study also found that **W** was larger near the ONH and at longer wavelengths, but did not depend on scattering angle or **T**. Because a 4.3° change in incident angle can change reflected intensity by a factor of 2.7, accounting for directional reflectance should improve the accuracy and reproducibility of RNFL reflectance measurements.

© 2015 Optical Society of America

OCIS codes: (170.4470) Ophthalmology; (170.4580) Optical diagnostics for medicine; (170.3660) Light propagation in tissues; (170.6935) Tissue characterization

References and links

1. D. Huang, E. A. Swanson, C. P. Lin, J. S. Schuman, W. G. Stinson, W. Chang, M. R. Hee, T. Flotte, K. Gregory, C. A. Puliafito, and J. G. Fujimoto, "Optical coherence tomography," *Science* **254**(5035), 1178–1181 (1991).
2. J. S. Schuman, M. R. Hee, C. A. Puliafito, C. Wong, T. Pedut-Kloizman, C. P. Lin, E. Hertzmark, J. A. Izatt, E. A. Swanson, and J. G. Fujimoto, "Quantification of nerve fiber layer thickness in normal and glaucomatous eyes using optical coherence tomography," *Arch. Ophthalmol.* **113**(5), 586–596 (1995).
3. J. S. Schuman, M. R. Hee, A. V. Arya, T. Pedut-Kloizman, C. A. Puliafito, J. G. Fujimoto, and E. A. Swanson, "Optical coherence tomography: a new tool for glaucoma diagnosis," *Curr. Opin. Ophthalmol.* **6**(2), 89–95 (1995).
4. G. Wollstein, J. S. Schuman, L. L. Price, A. Aydin, P. C. Stark, E. Hertzmark, E. Lai, H. Ishikawa, C. Mattox, J. G. Fujimoto, and L. A. Paunescu, "Optical coherence tomography longitudinal evaluation of retinal nerve fiber layer thickness in glaucoma," *Arch. Ophthalmol.* **123**(4), 464–470 (2005).
5. D. Huang and A. Kirschbaum, "Glaucoma diagnosis based on nerve fiber layer signal ratio in optical coherence tomography," presented at the Second Annual Meeting on Optical Coherence Tomography, Long Boat Key, FL2000.
6. M. E. Pons, H. Ishikawa, R. Gürses-Ozden, J. M. Liebmann, H. L. Dou, and R. Ritch, "Assessment of retinal nerve fiber layer internal reflectivity in eyes with and without glaucoma using optical coherence tomography," *Arch. Ophthalmol.* **118**(8), 1044–1047 (2000).
7. X.-R. Huang, Y. Zhou, W. Kong, and R. W. Knighton, "Reflectance decreases before thickness changes in the retinal nerve fiber layer in glaucomatous retinas," *Invest. Ophthalmol. Vis. Sci.* **52**(9), 6737–6742 (2011).
8. J. Dwell, S. Liu, B. Wang, A. McElroy, D. Ho, M. K. Markey, T. Milner, and H. G. Rylander 3rd, "Thickness, phase retardation, birefringence, and reflectance of the retinal nerve fiber layer in normal and glaucomatous non-human primates," *Invest. Ophthalmol. Vis. Sci.* **53**(8), 4380–4395 (2012).
9. J. van der Schoot, K. A. Vermeer, J. F. de Boer, and H. G. Lemij, "The effect of glaucoma on the optical attenuation coefficient of the retinal nerve fiber layer in spectral domain optical coherence tomography images," *Invest. Ophthalmol. Vis. Sci.* **53**(4), 2424–2430 (2012).

10. K. A. Vermeer, J. van der Schoot, H. G. Lemij, and J. F. de Boer, "RPE-normalized RNFL attenuation coefficient maps derived from volumetric OCT imaging for glaucoma assessment," *Invest. Ophthalmol. Vis. Sci.* **53**(10), 6102–6108 (2012).
11. S. K. Gardiner, S. Demirel, J. Reynaud, and B. Fortune, "Changes in retinal nerve fiber layer reflectance intensity are related to functional loss in glaucoma," *Invest. Ophthalmol. Vis. Sci.* **56**, 2057 (2015).
12. A. J. Weber, P. L. Kaufman, and W. C. Hubbard, "Morphology of single ganglion cells in the glaucomatous primate retina," *Invest. Ophthalmol. Vis. Sci.* **39**(12), 2304–2320 (1998).
13. T. Shou, J. Liu, W. Wang, Y. Zhou, and K. Zhao, "Differential dendritic shrinkage of alpha and beta retinal ganglion cells in cats with chronic glaucoma," *Invest. Ophthalmol. Vis. Sci.* **44**(7), 3005–3010 (2003).
14. T. Taniguchi, M. Shimazawa, and H. Hara, "Alterations in neurofilament light in optic nerve in rat kainate and monkey ocular hypertension models," *Brain Res.* **1013**(2), 241–248 (2004).
15. C. Balaratnasingam, W. H. Morgan, L. Bass, S. J. Cringle, and D.-Y. Yu, "Time-dependent effects of elevated intraocular pressure on optic nerve head axonal transport and cytoskeleton proteins," *Invest. Ophthalmol. Vis. Sci.* **49**(3), 986–999 (2008).
16. B. P. Buckingham, D. M. Inman, W. Lambert, E. Oglesby, D. J. Calkins, M. R. Steele, M. L. Vetter, N. Marsh-Armstrong, and P. J. Horner, "Progressive ganglion cell degeneration precedes neuronal loss in a mouse model of glaucoma," *J. Neurosci.* **28**(11), 2735–2744 (2008).
17. X.-R. Huang and R. W. Knighton, "Altered F-actin distribution in retinal nerve fiber layer of a rat model of glaucoma," *Exp. Eye Res.* **88**(6), 1107–1114 (2009).
18. M. Salinas-Navarro, L. Alarcón-Martínez, F. J. Valiente-Soriano, A. Ortín-Martínez, M. Jiménez-López, M. Avilés-Trigueros, M. P. Villegas-Pérez, P. de la Villa, and M. Vidal-Sanz, "Functional and morphological effects of laser-induced ocular hypertension in retinas of adult albino Swiss mice," *Mol. Vis.* **15**, 2578–2598 (2009).
19. C. T. Fu and D. Sretavan, "Laser-induced ocular hypertension in albino CD-1 mice," *Invest. Ophthalmol. Vis. Sci.* **51**(2), 980–990 (2010).
20. X. Huang, W. Kong, Y. Zhou, and G. Gregori, "Distortion of axonal cytoskeleton: an early sign of glaucomatous damage," *Invest. Ophthalmol. Vis. Sci.* **52**(6), 2879–2888 (2011).
21. R. W. Knighton, X. Huang, and Q. Zhou, "Microtubule contribution to the reflectance of the retinal nerve fiber layer," *Invest. Ophthalmol. Vis. Sci.* **39**(1), 189–193 (1998).
22. X.-R. Huang, R. W. Knighton, and L. N. Cavuoto, "Microtubule contribution to the reflectance of the retinal nerve fiber layer," *Invest. Ophthalmol. Vis. Sci.* **47**(12), 5363–5367 (2006).
23. B. Fortune, L. Wang, G. Cull, and G. A. Cioffi, "Intravitreal colchicine causes decreased RNFL birefringence without altering RNFL thickness," *Invest. Ophthalmol. Vis. Sci.* **49**(1), 255–261 (2008).
24. R. W. Knighton, C. Baverez, and A. Bhattacharya, "The directional reflectance of the retinal nerve fiber layer of the toad," *Invest. Ophthalmol. Vis. Sci.* **33**(9), 2603–2611 (1992).
25. R. W. Knighton and X.-R. Huang, "Directional and spectral reflectance of the rat retinal nerve fiber layer," *Invest. Ophthalmol. Vis. Sci.* **40**(3), 639–647 (1999).
26. R. W. Knighton and C. Qian, "An optical model of the human retinal nerve fiber layer: implications of directional reflectance for variability of clinical measurements," *J. Glaucoma* **9**(1), 56–62 (2000).
27. C. F. Bohren and D. R. Huffman, *Absorption and Scattering of Light by Small Particles* (John Wiley & Sons, 1983).
28. B. J. Lujan, A. Roorda, R. W. Knighton, and J. Carroll, "Revealing Henle's fiber layer using spectral domain optical coherence tomography," *Invest. Ophthalmol. Vis. Sci.* **52**(3), 1486–1492 (2011).
29. R. W. Knighton and X.-R. Huang, "Visible and near-infrared imaging of the nerve fiber layer of the isolated rat retina," *J. Glaucoma* **8**(1), 31–37 (1999).
30. X.-R. Huang and R. W. Knighton, "Microtubules contribute to the birefringence of the retinal nerve fiber layer," *Invest. Ophthalmol. Vis. Sci.* **46**(12), 4588–4593 (2005).
31. X.-R. Huang, and R. W. Knighton, "Fixed retina as a tissue phantom for the retinal nerve fiber layer," *Invest. Ophthalmol. Vis. Sci.* **42**, 694 (2001).
32. R. W. Knighton and Q. Zhou, "The relation between the reflectance and thickness of the retinal nerve fiber layer," *J. Glaucoma* **4**(2), 117–123 (1995).
33. Q. Zhou and R. W. Knighton, "Light scattering and form birefringence of parallel cylindrical arrays that represent cellular organelles of the retinal nerve fiber layer," *Appl. Opt.* **36**(10), 2273–2285 (1997).
34. R. M. Pasternack, J.-Y. Zheng, and N. N. Boustany, "Optical scatter changes at the onset of apoptosis are spatially associated with mitochondria," *J. Biomed. Opt.* **15**(4), 040504 (2010).
35. K. J. Chalut, J. H. Ostrander, M. G. Giacomelli, and A. Wax, "Light scattering measurements of subcellular structure provide noninvasive early detection of chemotherapy-induced apoptosis," *Cancer Res.* **69**(3), 1199–1204 (2009).
36. Y. Z. Spector, Q. Zhao, X. Zhao, W. J. Feuer, P. L. Maravich, and X.-R. Huang, "Classification of axonal subtypes based on cytoskeletal components," *Cell Health Cyto.* **6**, 1–10 (2014).
37. X.-R. Huang, H. Bagga, D. S. Greenfield, and R. W. Knighton, "Variation of peripapillary retinal nerve fiber layer birefringence in normal human subjects," *Invest. Ophthalmol. Vis. Sci.* **45**(9), 3073–3080 (2004).
38. B. Cense, T. C. Chen, B. H. Park, M. C. Pierce, and J. F. de Boer, "*In vivo* birefringence and thickness measurements of the human retinal nerve fiber layer using polarization-sensitive optical coherence tomography," *J. Biomed. Opt.* **9**(1), 121–125 (2004).

39. X.-R. Huang, Y. Z. Spector, X. Zhao, and Q. Zhao, "Birefringence of retinal nerve fiber layer: correlation with degrees of glaucomatous damage," *Invest. Ophthalmol. Vis. Sci.* **55**, 4774 (2014).
40. X.-R. Huang, Y. Z. Spector, and M. Castellanos, "Reflectance spectrum and birefringence of retinal nerve fiber layer in hypertensive retinas," *Invest. Ophthalmol. Vis. Sci.* **56**, 4557 (2015).
41. M. Sugita, M. Pircher, S. Zotter, B. Baumann, P. Roberts, T. Makihiro, N. Tomatsu, M. Sato, C. Vass, and C. K. Hitzenberger, "Retinal nerve fiber bundle tracing and analysis in human eye by polarization sensitive OCT," *Biomed. Opt. Express* **6**(3), 1030–1054 (2015).

1. Introduction

The retinal nerve fiber layer (RNFL), lying just under the retinal surface, consists of the axons of retinal ganglion cells. Assessment of the RNFL by optical methods is often used in clinical diagnosis of various retinal diseases. For instance, Optical Coherence Tomography (OCT), which is widely used in clinical diagnosis of glaucoma, measures RNFL thickness by identifying the RNFL as a highly reflective layer under the retinal surface, with change of thickness used as a biomarker for axonal damage [1–4].

Recent studies of glaucomatous retinas reveal that a decrease of RNFL reflectance occurs prior to thinning of the RNFL [5–11]. Glaucoma damages retinal ganglion cells (RGC) and their axons [12–20]. Elevation of intraocular pressure (IOP) causes shrinkage of RGC soma, alteration of axonal cytoskeleton and loss of RGC and axons. Importantly, alteration of axonal ultrastructure can occur before loss of axons [15,16,19,20]. It seems likely that RNFL reflectance depends directly on the ultrastructure of the ganglion cell axons. Supporting this idea, depolymerization of axonal microtubules (MTs) decreases RNFL reflectance [21–23]. Further, our recent *in vitro* study in hypertensive retinas shows that change of RNFL reflectance associates with axonal cytoskeletal alteration [7]. Because RNFL reflectance appears to be more sensitive to glaucomatous damage than change of RNFL thickness, direct measurements of RNFL reflectance hold promise as a method for the early detection of glaucoma.

Many of these RNFL reflectance studies were performed *in vivo* in humans and other primates and RNFL reflectance was derived from OCT images [5,6,8–10]. The reflected signal in an OCT image is related to the scattering properties of the RNFL and, in addition, depends on other factors, such as ocular media opacities and the intensity of the light beam that reaches the retina. To compensate the effects of these factors, the ratio of the OCT reflected signal within the RNFL to a reference layer was often calculated to normalize the reflectance of the RNFL alone [5,6,8–10]. Although this normalization may eliminate the effect of other factors on estimations of RNFL reflectance, directional reflectance of the RNFL could be a major source of variability for measured RNFL reflectance [24–26], and none of the *in vivo* studies took this variable into account. Angular measurements demonstrate that the reflectance of nerve fiber bundles is very directional, with the scattered light confined to a conical sheet coaxial with the bundles [24,25]. This directionality implies that the RNFL reflectance arises from light scattering by cylindrical structures [27]. The RNFL reflectance spectrum decreases with increase of wavelength in a way that implies a two-mechanism model of RNFL reflectance [25]. In this model, both thin and thick cylinders contribute to RNFL reflectance, with thin cylinders dominating the reflectance at short wavelengths and thick cylinders contributing more at longer wavelengths.

An evident example of directional reflectance of the RNFL appears in OCT cross-sectional images of the optic nerve head (ONH), where RNFL reflectance decreases rapidly and bundles disappear as the bundles turn and enter the optic nerve. Directional reflectance of oriented cylindrical structures has also been observed in OCT images of photoreceptor axons in Henle's fiber layer, which can appear or disappear depending on the position of the OCT beam in the pupil of the eye [28]. Hence, to accurately and reproducibly measure RNFL reflectance, directional reflectance of nerve fiber bundles must be taken into account.

Our previous studies used an *in vitro* preparation of the retina to investigate the directional reflectance of the RNFL, which allowed measuring the RNFL without the confounding effects

of the ocular media [24,25]. Those studies, however, measured the integrated reflectance of entire bundles, without regard to their thickness. The present study derives reflectance per unit thickness, a tissue property comparable to that measured by OCT, and extends our previous studies by providing quantitative comparisons of RNFL directional reflectance measured at different scattering angles, different distances from the ONH and on bundles with different thicknesses.

2. Methods

2.1 Preparation of isolated retina

Normal Wistar rats were used in the experiments because, as in humans, the axons in the rat RNFL are unmyelinated. The protocol for the use of animals was approved by the Animal Care and Use Committee of the University of Miami and procedures adhered to the Association for Research in Vision and Ophthalmology (ARVO) Statement for the Use of Animals in Ophthalmic and Vision Research. Tissue preparation followed previously developed procedures [29]. Briefly, the eye of an anesthetized rat was removed and the animal was euthanized. An eye cup of 5 mm diameter that included the optic nerve was excised and placed in a dish of a warm (33 – 35°C) oxygenated physiologic solution. The retina was dissected free of the retinal pigment epithelium and choroid and then draped across a slit in a black membrane with the photoreceptor side against the membrane. A second, thinner membrane with a slit matched to the black membrane was put on the RNFL surface to gently stretch the retina and eliminate wrinkles. The above procedure was carried out with intense white illumination, which thoroughly bleached the visual pigment in the photoreceptors and ensured that the reflectance in this layer remained constant. The mounted retina was placed in a chamber perfused with a warm oxygenated physiologic solution to maintain the tissue in a physiological condition that simulated the retina's *in vivo* state. The preparation took less than 10 minutes. The optical properties of such prepared retinas were stable for at least two hours [22,30].

Retinas fixed with 4% paraformaldehyde for 30 min were also used for the experiments that required manipulating the tissue to achieve specific orientation of nerve fiber bundles. Brief fixation does not appreciably change RNFL optical properties [31].

2.2 Multispectral imaging microreflectometer

The multispectral IMR (Fig. 1) is briefly described as follows [22,29]. A retina mounted in a chamber with a spherical window was illuminated by a monochromatic light source that used a tungsten-halogen lamp and interference filters. Filters were available for wavelengths ranging from 400 nm to 830 nm with 10 nm bandwidth at half-height. The retina was imaged by a camera consisting of an objective lens and a cooled charge-coupled device (CCD) (U47+ Digital Imaging System; Apogee Instruments, Inc., Logan, UT). The camera provided a resolution of 2.2 $\mu\text{m}/\text{pixel}$ and a field-of view of 2.3 \times 2.3 mm on tissue in an aqueous medium. The optical axes of the camera and light source coincided with the radii of a spherical coordinate system centered on the retina. The camera could be moved in azimuth with its elevation fixed at 13° below the system's equator, and the light source could be adjusted both in azimuth and elevation. The azimuth and elevation angles were read with 1° resolution and 0.5° precision.

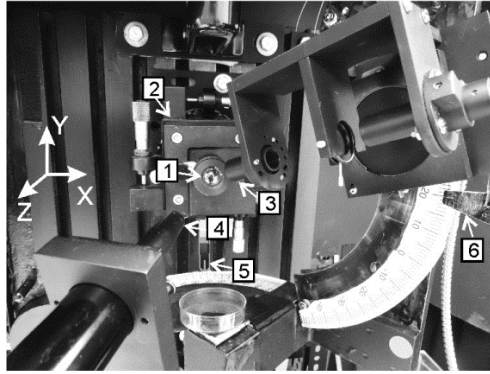


Fig. 1. Photograph of multispectral imaging microreflectometer (IMR). 1. Retinal chamber with a spherical window. 2. Translation and rotation stages for adjusting bundle position and orientation. 3. Light source probe. 4. Detection probe with a CCD camera (not shown). 5 and 6. Angle gauges for azimuth and elevation angles of the light source. Inset: the laboratory coordinate system.

2.3 Measurement of directional reflectance

The angular variation of the RNFL reflectance is consistent with light scattering by cylindrical structures in the RNFL [24,25]; hence the reflectance is very directional and confined to a conical sheet centered on the axes of the cylinders [27]. Figure 2(A) shows the unique geometry of light scattering by a single cylinder. The incident angle (θ) of a bundle was defined as the angle between the incident ray and a plane perpendicular to the bundle; the scattering angle (ϕ) was defined as the angle between incident and scattering planes, where the incident plane contained the incident ray and the bundle and the scattering plane contained the reflected ray and the bundle. For a single cylinder of infinite length, or a parallel array of such cylinders, the scattered sheet has infinitesimal thickness. For the RNFL reflectance, however, the misalignment of cylinders in bundles will broaden the scattered sheet and the finite apertures of the light source and camera will also spread the measured cone around its actual location (Fig. 2(B)). This study measured the angular spread function (ASF) of RNFL reflectance around the scattered cone to provide understanding of the dependence of RNFL reflectance value on geometric settings of measurements.

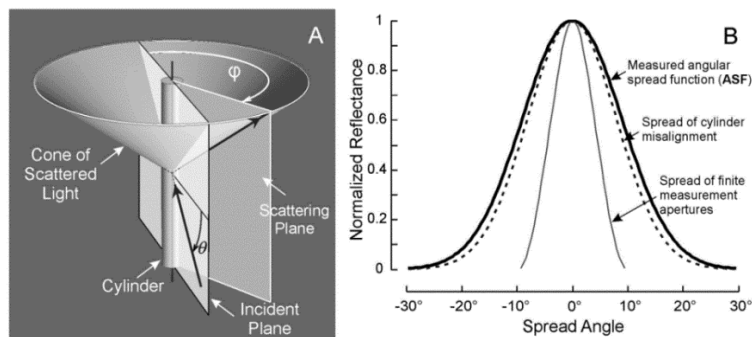


Fig. 2. (A) Geometry of light scattering by a cylinder. The light scattered by a cylinder is confined to a conical sheet coaxial with the cylinder axis. The apex angle of the cone is twice the angle between the cylinder axis and the incident ray. Definitions of the incident angle (θ), scattering angle (ϕ), and the incident and scattering planes are given in the text. (B) Illustration of angular spread functions. Misalignment of cylinders in a scattering array broadens the infinitesimally thin sheet shown in A. The finite apertures of the light source and camera also spread the measured cone. The actual measured spread function (ASF) is the convolution of the angular spreads due to cylinder misalignment and the finite apertures of the light source and camera.

The scattering depicted in the bundle coordinates of Fig. 2 was measured in the laboratory coordinates established by the IMR (Fig. 1). Because the geometry of Fig. 2(A) also works in reverse, in the experiments the light source probe was moved to probe the scattered cone while the camera position was fixed to achieve a constant relationship between the camera and the retina. The procedures for setting measurement geometry are as follows. Bundles were often oriented approximately vertically in the laboratory coordinate system. The azimuths of the camera and light source were adjusted to positions such that the background reflection was dark and uniform. The angular spread around a conical sheet was then measured by changing the elevation angle (Θ) of the light source. Values for θ and ϕ of a bundle were calculated from the positions of the light source and camera and the bundle orientation and position in the retina. The three-dimensional orientation of a bundle was calculated from its projected angles in images that were taken at two additional camera positions at the end of an experiment.

Note that the azimuths of the camera and light source, the elevation angle of the light source and bundle orientation were defined in laboratory coordinates (Fig. 1), whereas θ and ϕ of a bundle were defined in cylinder coordinates (Fig. 2(A)).

2.4 Calculation of RNFL reflectance

Black images taken with the same exposure duration but with the light source off were subtracted from each image to compensate for the dark current and bias level of the CCD. The resulting pixel values were directly proportional to reflected intensity. To calculate relative reflectance of the RNFL, images were also taken of a diffuse white reflector (Kodak 6080 White Reflectance Coating; Eastman Kodak Company, Rochester, NY). Pixel values of retinal images were then converted to relative reflectance R_λ by Eq. (1)

$$R_\lambda = \gamma_\lambda \frac{P}{P_w} \frac{t_w}{t} \quad (1)$$

where γ_λ is a known reflectance coefficient of the white reflector at wavelength λ , P and P_w are pixel values of the tissue and white reflector, respectively, and t and t_w are their corresponding exposure durations. Hereafter the relative reflectance is simply called reflectance.

To measure the reflectance of a nerve fiber bundle, rectangular areas were chosen both on the bundle and nearby gaps (retinal areas between bundles) and the reflectance of the pixels in each area were averaged [22,25]. The total pixels included for calculating a bundle reflectance ranged from 80 to 150, depending on bundle size (Examples of bundle and gap areas are shown in Fig. 4.) Reflectance measured on bundle areas included light reflected from the RNFL and from underlying tissue. Because the weak scattering of the RNFL caused little attenuation to an incident beam, we assumed that the reflectance from deeper layers was approximately the same as that from nearby gap areas. The average reflectance of gap areas, therefore, was subtracted from the total reflectance measured on the bundle areas to get an estimate of bundle reflectance alone. The reflectance of nearby areas on the same bundle was then averaged. To compensate possible tissue shift during measurements, an entire set of images was registered by horizontal and vertical translation.

2.5 Measurement of RNFL thickness

After optical measurements, the retina was fixed with 4% paraformaldehyde for 30 min at room temperature and then removed from the membranes for further immunohistochemical staining of axonal cytoskeleton and nuclei. The detailed staining procedures have been published previously [20]. The fluorescently-stained retina was imaged using a Confocal Scanning Laser Microscope (cLSM, Leica TCS SP5, Leica Microsystems). A 40 \times oil objective provided en face images of a retina with a resolution of 0.76 $\mu\text{m}/\text{pixel}$. At least a 3 \times

3 tiled array of images was taken that covered a retinal area of 1.2×1.2 mm with the ONH at the center (Fig. 3(A)). En face images were collected at evenly spaced positions in depth (1 μm apart in tissue) starting from the RNFL surface through the retina to a depth at least including the ganglion cell layer. The retina was then reconstructed in 3-D and cross-sectional images were synthesized from the reconstruction with customized software.

The en face confocal image of a retina was registered onto the reflectance image of the same retina by matching blood vessels (Fig. 3(A), 3(B)). The cross-sectional images of the bundles used for reflectance analysis were obtained from a reconstructed 3-D cLSM image (Fig. 3(C)). The RNFL was identified by the intensely stained axonal cytoskeleton at the top layer of the retina (staining of microtubules (MTs) is shown in Fig. 3(A), 3(C)). Boundaries of nerve fiber bundles were detected by image processing software followed by manual adjustments. The RNFL thickness profile along the cross-sectional image was then calculated (Fig. 3(D)). To measure the thickness (**T**) of a bundle, a window centered on the bundle was drawn with its width being approximately half the width of the bundle (dashed lines in Fig. 3(D)). The mean values of **T** within the window were calculated to represent the thickness of the bundle.

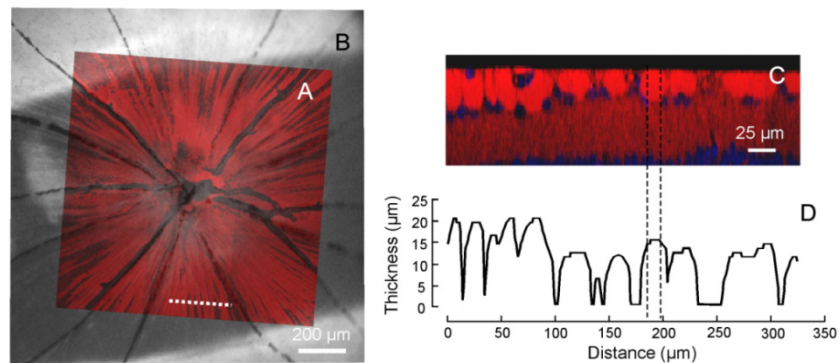


Fig. 3. Image registration and measurement of bundle thickness. (A) and (B) En face images taken by the confocal microscope and imaging microreflectometer. The confocal image (A) is registered onto the reflectance image (B) by matching blood vessel patterns. The confocal image shows stained microtubules (MTs) and is displayed as 60% transparency to reveal the underlying reflectance image. The reflectance image was taken at wavelength $\lambda = 440$ nm. (C) Cross-sectional image along the dashed line in (A). Red: stained MTs, blue: stained nuclei. (D) Bundle thickness measured from the image in (C). The vertical dashed lines show the window used for calculating bundle thickness.

2.6 Data analysis

The measured **ASF** of a scattered cone was the convolution of the actual spread and the instrument's angular response function, which was approximately 10° wide. We used a symmetrical decaying exponential to model the actual spread function to fit a measured **ASF**. Two parameters, the amplitude (**A**) of the exponential and its half-width (**W**), measured to $1/e$ of the peak, give a mathematical description of the data [25].

All data extraction and analysis programs were implemented in MATLAB (The MathWorks, Inc., Natick, MA).

2.7 Statistical analysis

The dependence of fitted **A** and **W** on studied variables was tested by a linear mixed model (LMM) analysis accounting for the correlation between multiple measurements made on the same bundles and post hoc least-significant difference (LSD) tests (IBM SPSS Statistics 22; IBM Corporation, Somers, NY). The significance level was set at $p < 0.05$.

3. Results

3.1 Directional reflectance of retinal nerve fiber bundles

As expected from previous work, the RNFL reflectance was very directional. An example is shown in Fig. 4. In this experiment nerve fiber bundles were oriented approximately vertically and measured near direct backscattering. At $\Theta = 20^\circ$ bundles appeared as bright stripes against a darker background (Fig. 4(A)), while at $\Theta = 45^\circ$ the same bundles were hardly discernible (Fig. 4(B)). Figure 4(C) shows the reflectance as a function of Θ with the peak reflectance at $\Theta = 20^\circ$. In contrast, the reflectance of nearby gap areas did not change much with Θ . Fitting the measured ASF with a symmetrical decaying exponential gave $A = 1.57 \pm 0.06\%$ and $W = 6.06^\circ \pm 0.11^\circ$ (value \pm SE of fit).

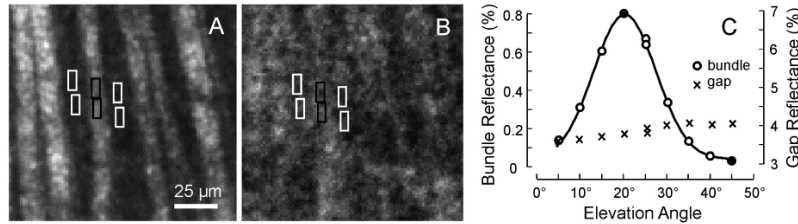


Fig. 4. Directional reflectance of retinal nerve fiber bundles. (A) Reflectance image of bundles measured at on-peak reflectance with the light source elevation angle $\Theta = 20^\circ$ and wavelength $\lambda = 500$ nm. Black boxes mark the areas on one bundle at which RNFL reflectance was analyzed. The incident angle θ and scattering angle ϕ for this area were 12° and 177° , respectively. White boxes mark the gaps between bundles; the reflectance of gap areas was used to estimate the reflectance of tissue underlying the bundle areas. (B) Image of the same retinal area shown in (A) but measured at off-peak reflectance ($\Theta = 45^\circ$) with $\theta = 22^\circ$ and $\phi = 178^\circ$. Bundles nearly disappear. Image contrast has been enhanced. (C) Angular spread of the marked areas in (A). The filled circles correspond to the images in (A) and (B). Gap reflectance did not change very much with the elevation angle of the light source. The total number of pixels for the bundle and gap areas was 100 and 180, respectively.

3.2 Dependence of angular spread function on scattering angles

To study whether a measured ASF depends on ϕ , a retina was rotated to allow measuring ASF of bundles at different ϕ . Manipulating tissues to measure specific bundles at different ϕ lengthened the duration of experiments. To remove temporal variation and ensure a reliable comparison of measured ASF, two fixed retinas were used to study the dependence of ASF on ϕ . Eight bundles, four from each of the retinas, were analyzed.

Figure 5(A) shows ASF of a bundle measured at $\phi = 141^\circ$, 153° and 172° with the corresponding $\theta = 12^\circ$, 14° and 15° when the bundle was measured at Θ of on-peak reflectance. Directional reflectance was observed at all studied ϕ . Shift of Θ for on-peak reflectance was due to the change of bundle position relative to the incident beam and camera position. Figure 5(B)-5(C) display the fitted A and W of eight bundles. All bundles showed that A increased with increase of ϕ . Grouping the data into ϕ ranges of $140^\circ - 148^\circ$ (ϕ_1), $157^\circ - 164^\circ$ (ϕ_2) and $172^\circ - 178^\circ$ (ϕ_3) showed that W was similar for $\phi_1 - \phi_3$ ($p = 0.19$, LMM analysis accounting for repeated measurements on the same bundles); however, comparing with ϕ_3 , which is near direct backscattering (180°), A decreased significantly at ϕ_1 and ϕ_2 ($p < 0.001$, LMM analysis and post-hoc LSD tests) with an average decrease of 3% at ϕ_2 and 10% at ϕ_1 .

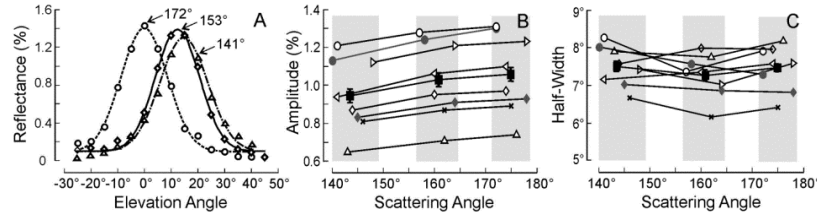


Fig. 5. Dependence of angular spread function on scattering angle. (A) Angular spread functions (ASF) of a bundle area measured at three ϕ . (B) and (C) Fitted magnitude A and half-width W of the ASF of eight bundles with each measured at three different ϕ . Gray bars show the grouping of the data based on ϕ . The black squares are the mean \pm SE of each group. θ at on-peak reflectance was between 12° and 20° . All bundles were measured at $r = 300 \mu\text{m}$ and $\lambda = 500 \text{ nm}$.

3.3 Angular spread function (ASF) along bundles

The angular spread of RNFL reflectance indicates misalignment of cylinders in a scattering array. To study whether such misalignment depends on bundle thickness, we further measured ASF along the same bundles at different distances (r) from the ONH center and on bundles with different thickness. Figure 6(A) shows ASF measured along a bundle with λ fixed at 500 nm. Fitted W (value \pm SE) was $11.09^\circ \pm 0.35^\circ$, $8.69^\circ \pm 0.18^\circ$ and $9.18^\circ \pm 0.27^\circ$ for $r = 200$, 300 and 400 μm , respectively. Peak reflectance decreased rapidly from $r = 200 \mu\text{m}$ to $r = 300 \mu\text{m}$ and then decreased more at $r = 400 \mu\text{m}$. Decrease of A related to T as shown in the corresponding cross-sectional image of the bundle (Fig. 6(B)). In this study ASF of 70 bundles from 14 retinas (4 – 6 bundles from each retina) were analyzed at $r = 200$, 300 and 400 μm . Their corresponding T was also measured. The relationship between A and T will be discussed in a later section. Table 1 summarizes the fitted A and W of 210 bundle locations with θ ranging from 4° to 22° and ϕ ranging from 162° to 179° . Along the same bundles W at $r = 200 \mu\text{m}$ was significantly higher than at $r = 300$ and 400 μm ($p < 0.001$, LMM analysis with bundle as a random effect and post-hoc LSD tests), that is, the spread was wider as the bundles neared the ONH. Among bundles with T ranging from 4.1 to 43.0 μm , however, W did not show correlation with T .

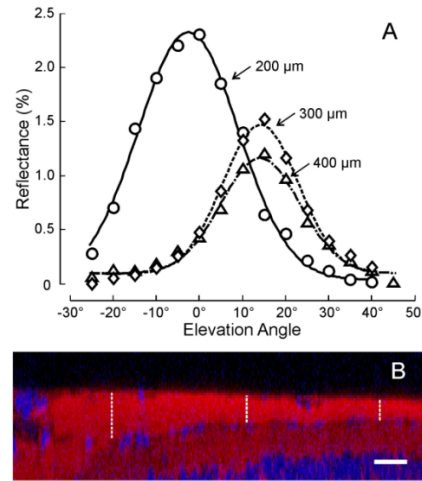


Fig. 6. Angular spread function along one bundle. (A) Angular spread functions measured along a bundle at the distances of $r = 200$, 300 and 400 μm from the ONH center and wavelength $\lambda = 500 \text{ nm}$. $\theta = 12^\circ - 14^\circ$ and $\phi = 171^\circ - 172^\circ$. (B) Cross-sectional image of the studied bundle in (A). Red: stained MTs, blue: stained nuclei. Vertical lines: bundle thickness at $r = 200$, 300 and 400 μm . Scale bar: 50 μm for horizontal and 25 μm for vertical.

Table 1 Angular spread function measured along bundles

r	200 μm	300 μm	400 μm
A	$1.73 \pm 0.75\%$	$1.23 \pm 0.73\%$	$0.93 \pm 0.50\%$
W	$8.96^\circ \pm 2.09^\circ$	$8.45^\circ \pm 1.94^\circ$	$8.50^\circ \pm 2.00^\circ$

Seventy bundles were analyzed; bundles were measured at wavelength $\lambda = 500$ nm; values of the fitted magnitude **A** and half-width **W** are mean \pm s.d.

3.4 Dependence of angular spread function on wavelength

Our previous experiments demonstrated that directional reflectance occurred at all wavelengths [25]. In this study ASF of the same 70 bundles in Table 1 was studied at wavelengths of 420, 500, 600, 700 and 830 nm. Table 2 summarizes the fitted **A** and **W** for each wavelength with **r** fixed at 300 μm . The fitted **A** decreased significantly with increase of λ ($p < 0.001$, LMM analysis with λ as a fixed effect and post-hoc LSD tests), while **W** was higher at the longer wavelengths (600, 700 and 830 nm) ($p < 0.001$). These results are consistent with our previous study.

Table 2 Average amplitude and half-width of angular spread functions at different wavelengths

λ	420 nm	500 nm	600 nm	700 nm	830 nm
A	$1.51 \pm 0.83\%$	$1.23 \pm 0.70\%$	$1.05 \pm 0.61\%$	$0.87 \pm 0.52\%$	$0.65 \pm 0.39\%$
W	$8.36^\circ \pm 1.81^\circ$	$8.45^\circ \pm 1.94^\circ$	$9.61^\circ \pm 1.92^\circ$	$9.58^\circ \pm 1.90^\circ$	$9.47^\circ \pm 1.85^\circ$

The same seventy bundles studied in Table 1; bundles were measured at distance **r** = 300 μm from the ONH center; values of the fitted magnitude **A** and half-width **W** are mean \pm s.d.

3.5 A tissue property: reflectance per unit thickness

In Fig. 6, we showed that **A** of the reflectance spread function decreased along the bundle with the decrease of **T** away from the ONH. Because in these en face images light scattering from the whole depth of a bundle contributes to measured reflectance [32], reflectance per unit thickness describes the RNFL reflectance property itself, which directly depends on its scattering structures. We calculated reflectance per unit thickness as the ratio of **A** and **T** and studied **A/T** along bundles and among bundles with various thicknesses. **A/T** of the 210 bundle locations is summarized in Table 3. Both **A** and **T** decreased with increase of **r**; however, **A/T** did not depend on **r** ($p = 0.78$, LMM analysis with retina and bundle as random effects, **T** as a covariate and **r** as a fixed effect), that is, for a specific bundle **A/T** did not depend on the location of a measured area along the bundle. In contrast, **A/T** varied significantly among bundles ($p < 0.001$). **A/T**, however, did not correlate to either **T** ($p = 0.66$) or retina ($p = 0.70$).

Because **A** is wavelength dependent, **A/T** also varied with wavelength. For all studied wavelengths, **A/T** did not vary along bundles. By averaging **A/T** measured at **r** = 200, 300 and 400 nm, the mean **A/T** was 0.866, 0.695, 0.059, 0.049 and 0.036%/ μm for $\lambda = 420, 500, 600, 700$ and 830 nm, respectively. The standard deviation of the mean was less than 0.002 for all λ .

Table 3 Reflectance per unit thickness at $\lambda = 500$ nm

r	200 μm	300 μm	400 μm
A	$1.73 \pm 0.75\%$	$1.23 \pm 0.73\%$	$0.93 \pm 0.50\%$
T	$24.91 \pm 9.98 \mu\text{m}$	$17.70 \pm 9.94 \mu\text{m}$	$13.39 \pm 6.73 \mu\text{m}$
A/T	$0.069 \pm 0.010\% / \mu\text{m}$	$0.070 \pm 0.0168\% / \mu\text{m}$	$0.069 \pm 0.010\% / \mu\text{m}$

The same seventy bundles studied in Table 1; values of the magnitude **A** and bundle thickness **T** are mean \pm s.d.

4. Discussion

Recent studies have shown that a decrease in RNFL reflectance occurs prior to thinning of the RNFL [5–11], and suggest that direct OCT measurement of RNFL reflectance may provide a powerful new method for the early detection of glaucoma. Although directional reflectance is a major source of variability for RNFL reflectance measurements [24–26], none of the *in vivo* studies took this into account. The present study confirms the dramatic impact of incident angle (θ) on RNFL reflectance and extends our previous work to different scattering angles (ϕ), different distances from the ONH and bundles with different thicknesses.

Parameter **W** in Table 1, calculated from data obtained with a fixed camera and moving light source, has a $1/e$ value of 8.5° for the decaying exponential used to characterize the bundle reflectance. This means that in an OCT measurement, where the entrance and exit beams are coincident and the fundus is measured at direct backscattering ($\phi = 180^\circ$), a change in θ of 4.3° away from the peak reflectance will cause a 2.7-fold decrease in intensity. In clinical practice, differences of 4.3° and much larger are easily encountered; for instance, 4.3° is the angle between the optic axis and an incident beam offset from the pupil center by 1.3 mm. In fact, the largest values for θ depend on a bundle's orientation relative to the pupil and thus on its location on the fundus. In addition, differences among individuals might be caused by differences in eye shape and axial length. A quantitative model displaying some of these effects has been published [26].

Figure 5 shows that **W** did not depend on ϕ and that **A**, the maximum (on-peak) reflectance of a nerve fiber bundle, decreased as ϕ moved away from direct backscattering. This dependence has no consequence for OCT, where $\phi = 180^\circ$. For optical devices with separate entrance and exit pupils, the limited pupil size in human eyes constrains ϕ to a maximum deviation of approximate $\pm 13^\circ$ from direct backscattering. Such a deviation would cause less than 3% change of RNFL reflectance (Fig. 5(B)) and, therefore, ϕ would not be a major contributor to the variation of RNFL reflectance.

It seems likely that the angular spread of bundle reflectance results from misalignment of scattering cylinders within the RNFL. On the hypothesis of cylinder misalignment, the fitted parameter **W** should relate to the degree of structural misalignment. At a fixed λ , **W** was larger for bundles near the ONH (Table 1), suggesting that scattering structures within the same bundle are better aligned in peripheral regions. **W** was also found to be wavelength dependent with **W** smaller at short wavelengths (Table 2). Because different scattering structures contribute to the RNFL reflectance and their contribution varies with wavelength [25], this result suggests that scattering structures that dominate RNFL reflectance at short wavelengths align better than those that dominate at long wavelengths. In addition to misalignment, scattering from truncated cylinders could also contribute to the angular spread of bundle reflectance. A $3\ \mu\text{m}$ long cylinder, for example, would have a spread of 6.3° at 500 nm. Mitochondria, ellipsoidal organelles oriented along axons, could be a candidate for such truncated cylinders [33,34]. The relationship between angular scattering and subcellular structure has been used to detect microstructural alteration in precancerous cells [34,35], so perhaps change of **W** under the development of glaucoma may be of interest for future studies.

Directional reflectance of the RNFL is a robust phenomenon seen *in vivo* and *in vitro*. Although isolated retinas were used in this study and axotomy could cause disorder of axonal ultrastructure, such disorder should only make RNFL reflectance less directional, and thus the values for **W** given in this study may present upper bounds on the angular spread of RNFL reflectance.

The fitted **A** of a measured **ASF** is an estimate of the maximum reflectance throughout the entire depth of a bundle. The ratio **A/T**, reflectance per thickness, is invariant of **T** and describes the same tissue property measured by OCT. In the present study of normal rat retinas, **A/T** was found to vary significantly among bundles, which suggests that the

ultrastructure contributing to RNFL reflectance is different among bundles. In contrast, A/T was constant along the same bundles. This result is consistent with our previous finding that the densities of axonal cytoskeletal components, F-actin, MTs and neurofilaments, do not vary significantly along bundles [36]. This result, however, is different from an *in vivo* study of normal human retinas by Vermeer, et al., which found that RNFL reflectance, calculated as an attenuation coefficient, decreases with increased distance from the ONH [10]. The discrepancy between these two studies could be due to a species difference, although birefringence is constant along bundles in both species [37–41]. It is more likely, however, that the reflectance variation along one bundle found by Vermeer, et al., is an indication of the effect of directional reflectance on their measurements, as predicted by the theoretical model developed by Knighton and Qian [26]. To examine this possibility we compared the azimuthal variation of RNFL attenuation coefficients reported by Vermeer, et al. to azimuthal variation calculated by Knighton and Qian [10,26]. The dashed line in Fig. 7 shows the variation of RNFL attenuation coefficients measured in a human eye on a 1 mm wide annulus around the ONH centered at a radius of 2.0 mm. This measured variation is very similar to the theoretically predicted variation on a 1.7 mm radius circle around the ONH (the solid line in Fig. 7), which solely results from changes of bundle orientation. Clearly, future research must rule out the effect of directional reflectance before other hypotheses are pursued.

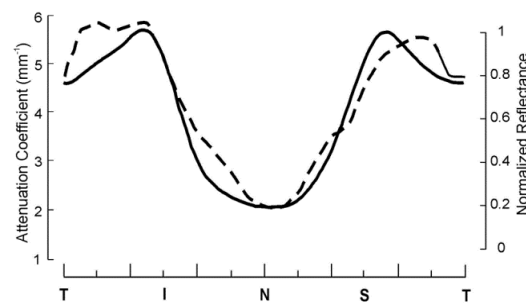


Fig. 7. Comparison of the azimuthal variation of RNFL attenuation coefficients measured in the human eye by Vermeer, et al. [10] (dashed line, left Y-axis) and RNFL reflectance calculated by Knighton and Qian [26] (solid line, right Y-axis). T: temporal; I: inferior; N: nasal; S: superior.

Application to future work, especially OCT, of the concepts presented here may be straightforward. It is important, however, to distinguish between research studies, in which time is available to explore sources of variance, and clinical practice, in which diagnostic information must be acquired with a minimum of auxiliary maneuvers. In the case of research, a possible impact of directional reflectance can be assessed by taking additional measurements with an offset entrance pupil, as was done by Lujan, et al., in their study of Henle's fiber layer [28]. In principle, several pupil positions could be used to map out the **ASF** for most of the RNFL, and the peak reflectance of bundles at different locations could be compared directly. In the case of clinical practice, which ideally should require only a single scan, the incident angle at a particular location might be calculated from the 3-D orientation of the retinal surface and knowledge of the transverse orientation of the RNFL. The incident angle could then be combined with values of the **ASF** from a normative dataset to correct the measured reflectance for the effect of directionality. If OCT measurement of RNFL reflectance provides early detection of glaucoma, as promised by recent studies, these extra analyses may well be worth the effort required.

Acknowledgments

This study was supported by NIH grant R01-EY019084, NIH center grant P30-EY014801 and an unrestricted grant from Research to Prevent Blindness, Inc.